TECHNICAL ARTICLE

Dry Sliding Wear Characteristics of NiP/TiN Duplex Coated Aluminum Alloy and Wear Analysis Using Response Surface Method

Farideh Davoodi, Masoud Atapour, Fakhreddin Ashrafizadeh, and Reyhaneh Rikhtehgaran

In this work, the effects of applied load, sliding velocity, and sliding distance on the tribological characteristics of 6061 aluminum alloy coated with NiP/TiN duplex coating were experimentally investigated and simulated by Response Surface Methodology (RSM). Dry sliding wear tests were conducted using a ball-on-disc apparatus. A developed model was proposed to predict the wear depth and friction coefficient of the coated specimens. According to the outcome of developed model, coefficient of determination values of 99.95 and 94.39% were obtained for the wear depth and friction coefficient, respectively. Scanning electron microscopy (SEM) examination of the worn surfaces after 500 m sliding revealed slight wear on the surface of the duplex coating under 2 N load (with the final friction coefficient of 0.35). By increasing the load to 7 N, heavier wear was observed, and the final friction coefficient was increased to 0.5. At the load of 12 N, both TiN and NiP layers were removed, and the final friction coefficient of 0.8 was recorded. Ultimately, wear analysis using RSM revealed that the applied load was the most important factor influencing the wear depth and friction coefficient of the coated specimens.

1. Introduction

Aluminum and its alloys are widely used in many applications, including aerospace, automotive, electronics, and marine industries, because of their high strength-to-weight ratio, favorable mechanical properties, and excellent corrosion resistance (Ref 1-3). However, the use of these alloys is often restricted in different applications due to their poor wear resistance (Ref 4, 5). According to the literature, the use of surface modification treatments is a promising technique to improve the wear behavior of aluminum alloys (Ref 6-9). Among the various coating techniques, physical vapor deposition (PVD), especially cathodic arc deposition, has been successfully applied to enhance the surface properties of aluminum alloys. It has been reported that the deposition of TiN coating using the PVD process can improve the hardness and wear resistance of aluminum alloys (Ref 10, 11). However, the deposition of TiN as a hard coating material on the soft aluminum substrates can be associated with a low load-bearing capacity (Ref 12, 13). It has been well known that the use of an intermediate layer between the hard coating and soft substrate is an important and useful strategy to improve the load-bearing of these coatings (Ref 14).

According to the literature, electroless nickel-phosphor (NiP) plating is one of the coating procedures for improving the adhesion and hardness of the PVD top layers (Ref 15). Also, using NiP interlayers can prevent the cracking of the top PVD coatings (Ref 16).

It has been reported that the use of Ni interlayer can improve the tribological performance (Ref 13, 15, 17, 18) and/or enhance the corrosion resistance (Ref 19) of the PVD coatings. Many investigations have been performed to fabricate interlayers before PVD coating on steels substrates. However, limited works have been conducted to investigate the role of NiP interlayers on the tribological performance of the PVD-coated aluminum substrates. In the work by Staia et al. (Ref 15), it has been reported that NiP/DLC duplex coatings on 2024-T3-aluminium alloy substrate exhibited a satisfactory wear behavior when the thickness of the NiP layer is higher than 60 μm. In another attempt by Wilson et al. (Ref 13), it has been demonstrated that the adhesion and wear resistance of the PVD CrN and CrAlN coatings on Cu substrate were improved by using an intermediate NiP layer. In another study carried out by Lin et al. (Ref 17), the Ni/CrN/ZrN multilayer coating reduced the friction coefficient and wear rate of ductile iron. Also, they reported that the multilayer coatings exhibited higher hardness (31.1 GPa) and elastic modulus (256.4 GPa).

A better understanding of the interaction of the factors affecting the wear performance of the coated specimens is an important research field. In this context, Response Surface Methodology (RSM) is reported to be one of the modern modeling techniques in expanding a suitable estimation method (Ref 20, 21). This method works based on the statistical and mathematical approaches (Ref 22, 23). Statistical design of

Farideh Davoodi, Masoud Atapour, and **Fakhreddin Ashrafizadeh**, Department of Materials Engineering, Isfahan University of Technology, 84156-83111 Isfahan, Iran; **Reyhaneh Rikhtehgaran**, Department of Mathematical Sciences, Isfahan University of Technology, 84156-83111 Isfahan, Iran. Contact e-mail: m.atapour@cc.iut.ac.ir.

experimental methods can lead to developing an empirical approach for wear examinations (Ref 24, 25). Several authors have investigated the analysis of the wear performance by using the RSM method. For example, Saravanan et al. (Ref 26) focused on the wear behavior of TiN coating on 316L by experimental methods and a regression model. They reported that both the regression model and experimental results showed an increase in the wear rate with increasing the load and velocity. In a newer study, Saravanan et al. (Ref 27) developed the RSM to simulate the wear behavior of a hybrid polymer biocomposite (UHMWPE) against TiN surface. They found that the higher applied load led to higher wear depth and higher friction coefficient. Furthermore, RSM has been used for simulating the wear performance of different Al-based composites (Ref 22).

The wear behavior of the electroless/TiN coatings has been investigated by Leyland et al. (Ref 28) and Subramanian et al. (Ref 29) for the steel and brass, respectively. However, the wear mechanisms were not addressed in these works. Also, the hardness of the substrate and the adhesion of the coating to the substrate are important factors influencing the load capacity and wear of coated samples (Ref 29). To the best of our knowledge, there is no information on the tribological behavior of duplex electroless/TiN coatings on aluminum substrates. Therefore, it is necessary to systematically study the wear and load ability of the duplex coatings on the aluminum-based substrate as a soft substrate. Also, linking the experimental results obtained from the wear examinations to the simulation data of RSM can be beneficial for determining the role of key parameters (applied load, sliding speed, and sliding distance) on the wear performance of the electroless/TiN coatings.

This study aimed to investigate the wear resistance and load-bearing behavior of NiP electroless/TiN PVD coating on Al 6061 substrate. In this work, electroless and PVD techniques were applied as two facile and cost-effective methods for fabricating a wear-resistant coating on aluminum-based substrates. In a particular work, the influence of load, sliding velocity, and sliding distance on the wear behavior of the NiP/TiN coated specimens were simulated by RSM and discussed based on the experimental results.

2. Experimental Details

2.1 Materials

In this study, disc specimens of AA 6061-T6 aluminum alloy with a diameter of 50 mm and a thickness of 5 mm were used as the substrates. A chemical analysis of the base material was conducted using a quantometer (ARUN-2500, Arun Company, UK). The chemical composition of aluminum alloy in weight percentage was Mg-1.0, Fe-0.65, Si-0.60, Cr-0.35, Cu-0.20, Zn-0.20, Mn-0.15, Ti-0.13, and Al-balance. The standard deviation for all elements was $< 1\%$. Before the coating treatments, the substrates were grounded and polished to a surface roughness of 0.05 ± 0.001 μm (R_a value) and degreased, rinsed with ethanol, and dried in the atmosphere.

2.2 Coating Treatment

The electroless NiP layer with a thickness of ~ 25 μm was plated on the smooth aluminum substrates. The aluminum substrates were subjected to the following pre-treatments before

Table 1 Chemical composition of electroless plating

Composition	Concentration
$C_4H_6O_4$	20 g/L
$C_3H_6O_3$	7 g/L
$NaH_2PO_2 \cdot H_2O$	30 g/L
$NiSO_4 \cdot 7H_2O$	31 g/L
$Na_3C_6H_5O_7$	5 g/L
Thiourea	2 mg/L
NaOH	8 g/L

Table 2 Process parameters of PVD coating

Process parameter	Value
Chamber pressure before deposition, mm bar	8×10^{-5}
Substrate bias voltage, V	100
Rotational speed of the substrate, rpm	10
Temperature during coating process, °C	120 ± 10
Deposition time, min	300
Sputtering time, min	20
Arc current, A	120
Distance between the sample and target, cm	30

the coating process: (i) ultrasonic cleaning in absolute ethanol at 25 °C for 10 min, (ii) alkaline cleaning of the surfaces in NaOH (50 g/L) at 70 °C for 1 min, (iii) acid pickling in acidic solution (55 mL HNO₃, 20 mL H₂SO₄, 25 mL HF) at 25 °C for 1 min, (iv) immersion in zincate solution at 25 °C for 15 s, (v) activation in HCl (30 vol.%) at 25 °C for 30 s, (vi) immersion in zincate solution at 25 °C for 20 s, and (vii) immersion in SLOTONIP 70 A solution for coating treatment. Between each step, the samples were washed with distilled water. In this work, the SLOTONIP 70 A solution (the commercial solution for electroless treatment) was purchased from Schlotter Company (Geislingen, Germany). The bath composition is presented in Table 1. The electroless NiP coating was deposited at a rate of 18-22 μm/hr in a mechanically stirred bath (750 rpm, pH: 4.7 ± 0.1) at 85–90 °C temperature for 75 min. The deposition rate was fixed according to the manufacturer's instructions. To improve the adhesion, hardness, and wear resistance of the coatings, the specimens were heat-treated at 400 °C for 1 hr, as reported by others (Ref 30). It has been reported that the heat treatment up to 400 °C is associated with increasing the hardness of the medium-phosphorus coatings (Ref 31).

In the next step, TiN coatings were deposited on the NiP coated substrates using PVD treatment. The thickness of the PVD layers was about 5 μm. TiN thin film was deposited as the topcoat by cathodic arc deposition process using titanium (purity > 99.5 wt.%) target in the argon (99.99%) and nitrogen (99.99%) mixed atmosphere. The details of the process parameters of TiN coating are presented in Table 2.

2.3 Characterization

To evaluate the hardness of the top surfaces of uncoated Al substrate, single electroless coating, and NiP/TiN duplex coating, a Vickers micro-hardness tester (Load: 100 mN, model: Leitz Wetzlar) was employed at room temperature.

Table 3   Inputs and their levels in CCD experimental plan

S. no	Factors	Designation	Levels* − 1.681	− 1	0	+ 1	+ 1.681
1.	Load, N	A	2	4	7	10	12
2.	Sliding velocity, m/s	B	0.016	0.05	0.1	0.15	0.184
3.	Sliding distance, m	C	163.64	300	500	700	836.36

* $\alpha = 1.681$

Also, to obtain the cross-section hardness profile of the duplex coated sample, nanoindentation tests were conducted using a TriboScope® system (Load: 7 mN, Hysitron, USA), equipped with a Berkovich-type indenter tip. This method has also been noticed in a previously published work (Ref 32) to measure the cross-section hardness of the electroless coatings with a thickness of ~ 20 μm. Surface roughness of the specimens was also measured using a Surftest SJ-201 (Mitutoyo) pro-filometer. Average values of the hardness and roughness were obtained from five measurements on each sample. The thickness and surface morphology of the duplex coating was obtained by using a Scanning Electron Microscopy (SEM, Philips XL30) equipped with an Energy-dispersive x-ray Spectroscopy (EDS). x-ray diffraction (XRD) pattern of the duplex coating was also obtained using an x-ray diffractometer (XRD, Philips XPERT-MPD) with Cu K_{α} radiation to identify the coating structure at 40 kV and 30 mA in the scanning angular (2θ) range from 10° to 100° with step size 0.05°, and 1 s counting time per step.

2.4 Wear Tests

A ball-on disk wear machine was used to conduct dry sliding wear tests. During the tests, a zirconia ball with a diameter of 10 mm and a hardness of 13.5 GPa was used. Before testing, the balls were cleaned with acetone. All the wear tests were repeated three times at room temperature and ambient humidity to ensure their repeatability. A set of trial experiments was conducted as follows: load from 4 to 10 N; sliding speed from 0.05 m/s to 0.15 m/s, and sliding distance from 300 to 700 m. According to the preliminary examinations of the coating, different and comparable results were obtained by these parameters. The wear depth of the worn surfaces was examined by a surface roughness tester (Mitutoyo model Sj-201, Japan). Five measurements were conducted on each sample and the average results were reported. The mean coefficient of friction (COF) was determined from the average values in the friction-distance curves. The morphology of the worn surfaces was studied using an SEM (Philips XL30). The corresponding samples were named Al (bare aluminum), Al/NiP (aluminum with NiP coating), and Al/NiP/TiN (duplex coating), respectively.

2.5 Response Surface Method

In this study, A: load (X_1), B: sliding velocity (X_2), and C: sliding distance (X_3) were selected as input parameters. The response surface functions 'R' representing the wear depth and COF were defined by the following equations (Ref 26):

$$\text{Wear depth} = f(A, B, C) \qquad \text{(Eq 1)}$$

Table 4   Variables and experimental results of the responses in actual values

Run. no.	Load, N	Sliding velocity, m/s	Sliding distance, m	Wear depth, μm	COF
1	10	0.05	700	33.2	0.63
2	10	0.15	700	27.8	0.54
3	4	0.05	300	8.9	0.29
4	4	0.15	300	8.1	0.31
5	4	0.15	700	10.8	0.28
6	12	0.1	500	32.5	0.68
7	2	0.1	500	6.2	0.27
8	10	0.15	300	16.2	0.35
9	7	0.1	500	14.7	0.42
10	4	0.05	700	10.6	0.31
11	7	0.1	500	14.5	0.46
12	7	0.1	500	14.5	0.40
13	7	0.1	500	14.4	0.38
14	7	0.1	500	14.3	0.47
15	7	0.016	500	17.4	0.40
16	7	0.1	500	14.7	0.37
17	7	0.184	500	12.9	0.39
18	7	0.1	836.36	22.5	0.39
19	10	0.05	300	21.6	0.42
20	7	0.1	163.64	10.8	0.27

$$\text{COF} = f(A, B, C) \qquad \text{(Eq 2)}$$

$$R = \beta_0 + \sum \beta_i X_i + \sum \beta_{ii} X_i^2 + \sum \beta_{ij} X_i X_j + \varepsilon \qquad \text{(Eq 3)}$$

where β_0 is a constant sentence, the coefficients β_i, β_{ii}, and β_{ij} are coefficients of the linear sentences, quadratic sentences, and the interaction sentences, respectively, and ε is the error of the model.

In this work, response surface methodology with central composite design (CCD) was selected to analyze the wear results. There are five levels of each variable in CCD: $(-\alpha, -1, 0, +1, +\alpha)$ (Ref 33). 95% confidence level was considered for all the coefficients based on the statistical analysis by using Minitab 19 package. Table 3 shows the factors and levels of the wear process. The experimental results of the wear depth and COF for 20 experiments are presented in Table 4.

The adequacy and significance of the used models were checked using analysis of variance (ANOVA). Mathematical modeling was developed to correlate each response with the wear parameters. Normal plots were used to assess the effect of each factor. Finally, counterplots were used to identify the responses based on different combinations of independent variables.

3. Results and Discussion

3.1 Microstructure

The surface morphology of Al 6061 coated with the NiP interlayer and TiN top layer is shown in Fig. 1a. The presence of some white and spherical particles can be due to the formation of the micro-droplets and pin-holes on the surfaces. These defects are known as the common features of the coatings produced by PVD-arc treatment. Droplets are formed as a result of ejection of liquid metal particles from the target material (Ref 34). These micro-droplets exhibit poor adhesion to the surface. Furthermore, de-bonding of the micro-droplets can lead to the formation of pinholes (Ref 35). According to the cross-section image of the duplex coating in Fig. 1b, it can be seen that uniform layers with the mean thickness of around 25 and ~ 5 μm were formed for NiP and TiN coatings, respectively. It is clear that a compact NiP coating was formed. Also, no porosity was detected in the interface of the coatings.

Figure 2 shows the XRD pattern of the fabricated NiP/TiN coating. Crystallized phases including Ni and Ni_3P were observed in the XRD spectrum, as confirmed by previous works (Ref 16, 18). It needs to note that the transformation of the amorphous phase to the crystalline phase led to the formation of the tetragonal intermediate phase (Ni_3P) (Ref 36). Also, the existence of Al peaks can be related to the base metal. It has been reported that the formation of TiN peaks is a sign of thermal and structural stability of the top layer (Ref 16).

3.2 Hardness and Surface Roughness

The results of the hardness and roughness evaluations are presented in Fig. 3. As shown in Fig. 3(a), the hardness of the top surface of the multilayer coating was higher than the subsurface, which is attributed to the formation of NiP/TiN coating. It has been reported that the load-bearing capacity of the duplex coating can improve by enhancing the hardness (Ref 13). The SEM images of the Vickers indentations were obtained from the top surface of different specimens and presented in Fig. 4. The indentation size was increased from 19.6 μm for Al/NiP/TiN to 52.4 for the uncoated substrate. No cracks were detected at the corners of the indentations. The hardness profile of the cross-section of Al/NiP/TiN coating is presented in Fig. 5. As can be seen, the surface hardness of ~ 0.85 GPa for the aluminum base metal was increased to 10 GPa for the NiP layer and then enhanced to ~ 22 GPa for the top layer of TiN.

According to Fig. 3(b), the Al/NiP/TiN specimen exhibited the highest roughness. The increasing of the roughness can be attributed to the sodium hypophosphite used for electroless treatment (Ref 37, 38) and the formation of macro-particles on the surface during the cathodic arc deposition process (Ref 19, 39).

3.3 Tribological Properties

Figure 6 shows the variation in the friction coefficient of the duplex-coated specimen with the sliding distance of 500 m and sliding velocity of 0.1 m/s, at three different loads. In order to
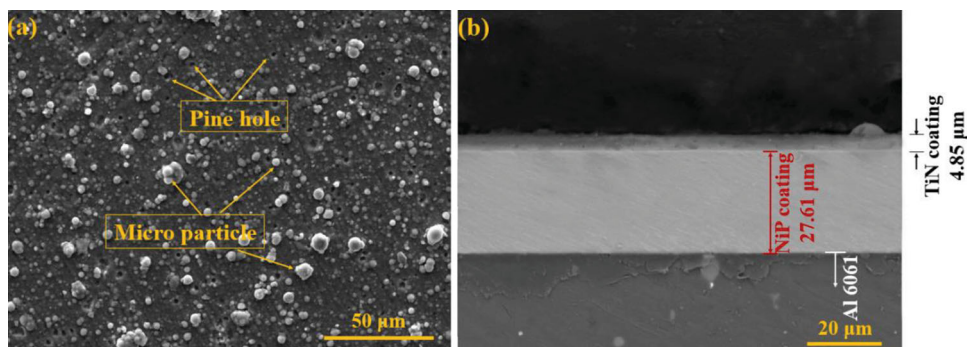

Fig. 1 (a) Surface morphology and (b) cross-section of the TiN coating on the 6061 aluminum alloy with the NiP interlayer
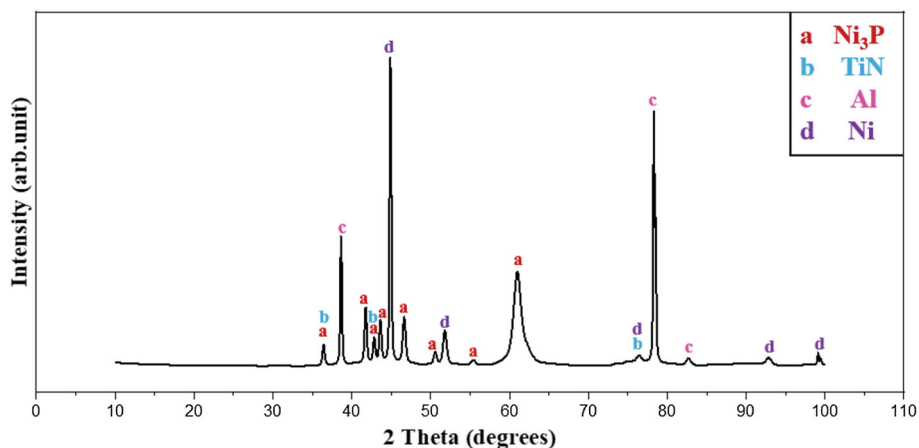

Fig. 2 XRD pattern of the TiN coating on the 6061 aluminum alloy with the NiP interlayer
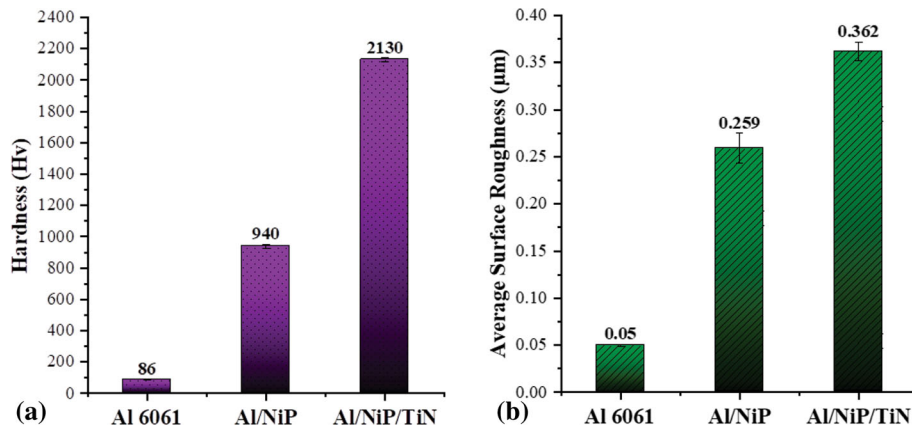
Fig. 3 Comparison of (a) hardness and (b) surface roughness of the samples
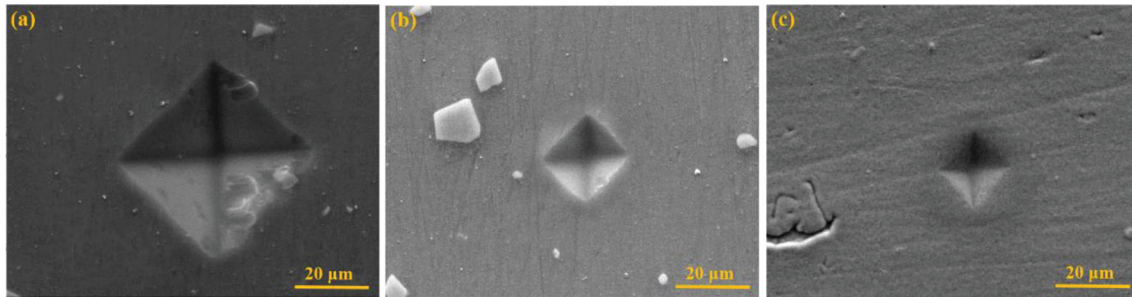

Fig. 4 SEM images of the micro-hardness indentations, (a) Al 6061, (b) Al/NiP, and (c) Al/NiP/TiN
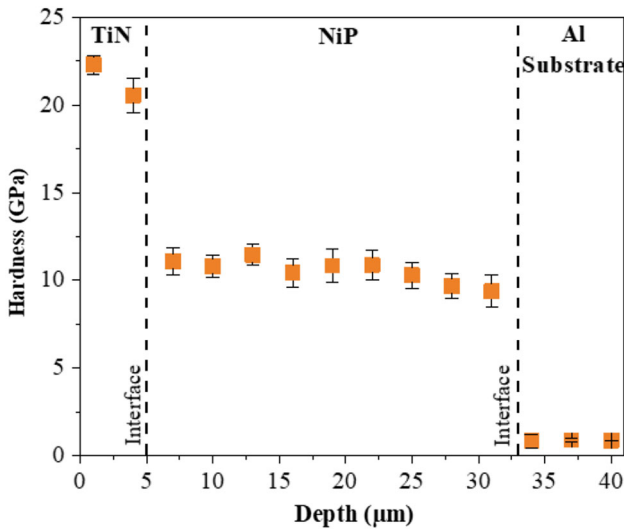

Fig. 5 Hardness profile of the cross-section of Al/NiP/TiN
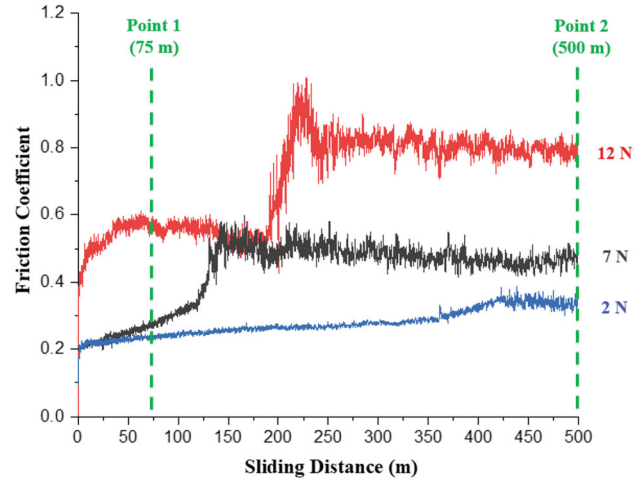

Fig. 6 The friction coefficient during the 500 m sliding at 0.1 m/s velocity and under loads of 2 N, 7 N, and 12 N

obtain more details of wear mechanism by SEM observation of the wear tracks, the test was repeated in similar conditions but with a sliding distance of 75 m. The worn surfaces of the duplex-coated sample under various loads after a sliding distance of 75 m and 500 m are shown in Fig. 7 and 8, respectively. EDS spectra relevant to the blue box region of each sample has also been presented. Under a load of 2 N, the friction coefficient of TiN was about 0.2 at the beginning and got more significant with increasing the sliding distance. According to Fig. 7(a), it can be seen that the surface was free

from tracks and other defects after 75 m sliding. The presence of TiN was confirmed using EDS result (Fig. 7a´). The TiN coating remained intact for 360 m and was stable without fluctuations. After that, the COF started to increase (∼ 0.35) with much oscillation due to TiN degradation. The low load of 2 N after 500 m sliding produced a relatively smooth wear track, as shown in Fig. 8(a). After around 425 m sliding, the COF was increased due to removing the TiN. The degradation of TiN coating was confirmed by the presence of 73.63 wt.% Ni element in EDS result. The less fluctuation of the friction
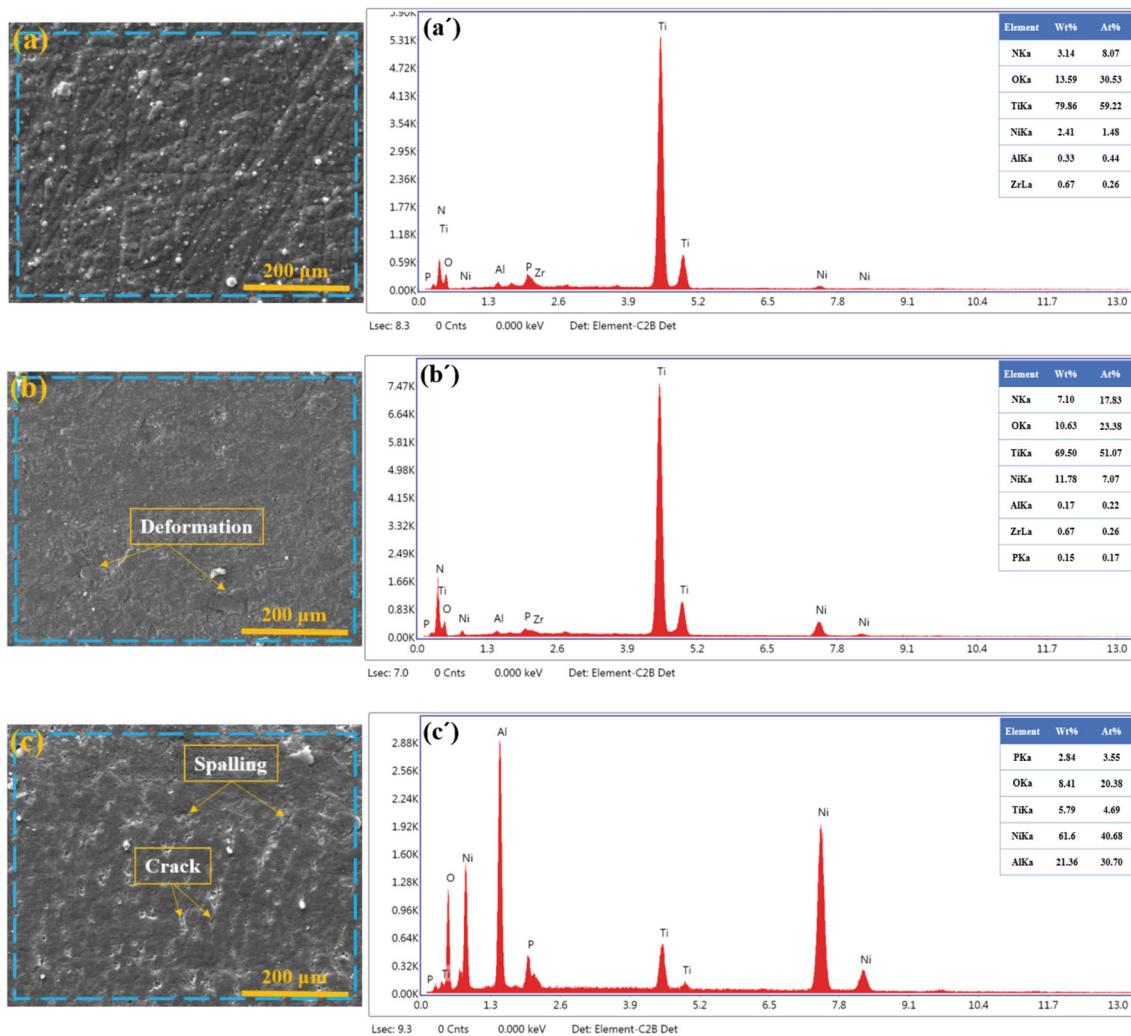
Fig. 7 Wear track morphologies (SEM images) and EDS of the worn surfaces during the 75 m sliding at 0.1 m/s velocity under (a, a´) 2 N, (b, b´) 7 N, and (c, c´) 12 N loads after sliding against the zirconia ball.

coefficient at 2 N load was caused by fewer plowing grooves during the wear process. In contrast, an increase in temperature at the interface and spots of severe deformation under high levels of load led to more fluctuation.

When the load was increased to 7 N, the COF was gradually raised from 0.2 to 0.3 after 100 m of sliding due to the decreasing thickness of TiN coating over time, similar to the friction coefficient of the TiN coating against the alumina ball (Ref 40). After 75 m sliding, no significant changes were observed. After 100 m sliding, the COF started increasing with a steeper slope until an almost sudden rise of ~ 0.5 was observed. Such a rapid increase of COF represented the failure and delamination of the TiN film. The steady-state COF values (about 0.45–0.5) were similar to those reported for NiP coatings investigated under similar friction conditions (Ref 15). The friction coefficient of the NiP coating at 7 N load was more than that of under 2 N load. Previous studies have also reported an increase in the friction coefficient of electroless coatings with load (Ref 41-43). It can be seen from Fig. 8(b) that the contact surface of the ball was increased by increasing the load. The higher magnification image showed the presence of cracks and fractures on the worn surface. The cyclic nature of the load can lead to the formation of cracks on the surface of the coating. It

is well known that the strain accumulation contributes to opening the cracks and forming rougher surfaces (Ref 44). The existence of the cracks and detached areas on the worn surface can increase the fatigue wear (Ref 45). Also, the deformation of colonies in the worn surface indicated the adhesive wear mechanism (Ref 46). The traces of plastic deformation of the coating were observed in Fig. 8(b). Some lips, ups, and downs on the worn surface indicated plastic deformation during the sliding test (Ref 47). This phenomenon was similar to the findings of Soleimani et al. (Ref 48) on the wear investigation of electroless NiP coating on aluminum 6061 under 8 N load. The presence of Al in the EDS of this worn surface indicated that the destruction had reached the substrate in some regions. The existence of Ti in the EDS results confirmed that TiN debris was formed during wear.

Assessment of the friction coefficient during the dry sliding test at 12 N load indicated that the TiN thin film was completely removed in the first steps of the test. On the other hand, the friction coefficient of 0.5-0.55 for the 200 m sliding means the NiP layer was still on the surface after removing the TiN coating. The worn surface of NiP coating and EDS result with 61.6% in the weight ratio of Ni element can be observed in Fig. 7(c), c´ after 75 m sliding. The increase in the friction
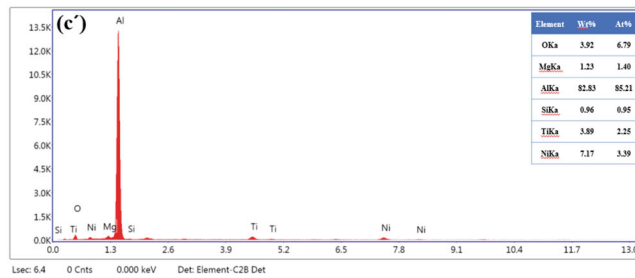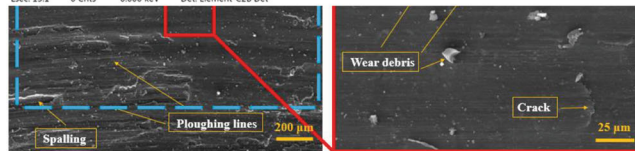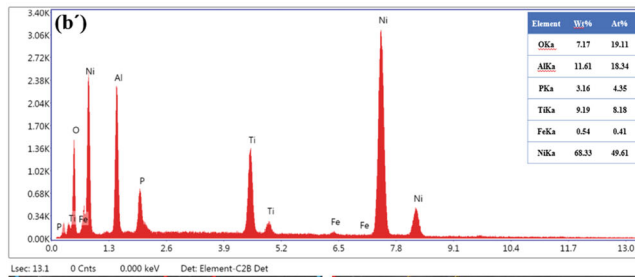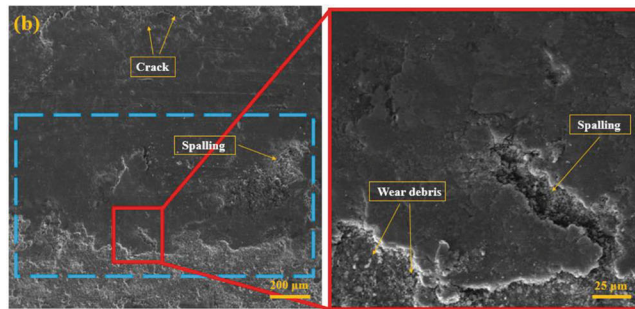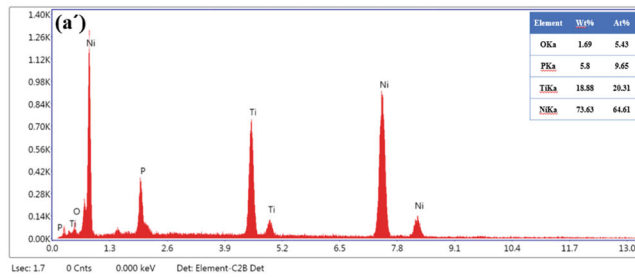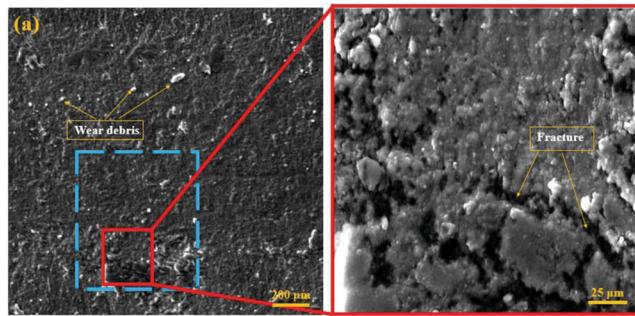
Fig. 8 Wear track morphologies (SEM images) and EDS of the worn surfaces during the 500 m sliding at 0.1 m/s velocity under (a, a´) 2 N, (b, b´) 7 N, and (c, c´) 12 N loads after sliding against the zirconia ball
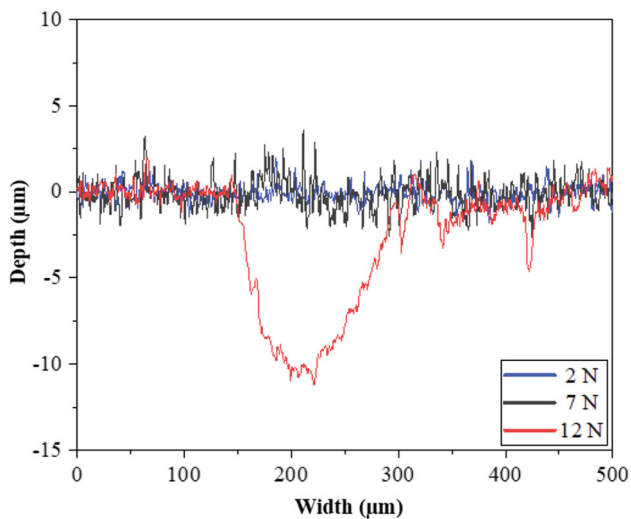
Fig. 9 Wear depth profiles during the 75 m sliding at 0.1 m/s velocity and under (a) 2 N, (b) 7 N, and (c) 12 N loads

coefficient of NiP coatings by increasing the load can be explained based on the increase in the contact area between the zirconia ball and coating surfaces (Ref 49). After 200 m sliding, the sudden change in the friction curve suggested that the failures in the NiP interlayer had occurred. After that, the COF values were stabilized at ∼ 0.8 and remained constant with considerable fluctuation. The sample showed severe wear, grooves and plowed surface, debris, delamination, and spallation on the surface after 500 m sliding (Fig. 8(c). It can be deduced that abrasive wear was the main mechanism for the whole wear process of the sample. The intensive Al peak in the EDS results of the worn surface (Fig. 8c´) indicated the severe damage of the coating and the appearance of the substrate during the wear. The presence of parallel grooves and scratches in the wear track can be due to the activation of the abrasive mechanism (Ref 46). It needs to note that the hardness of the surface was increased due to the re-compacting of debris (Ref 15). The higher load encouraged the plowing on the surfaces. Also, the formation of irregular cracks can increase due to the activation of bending stresses (Ref 50). These cracks, plowing,
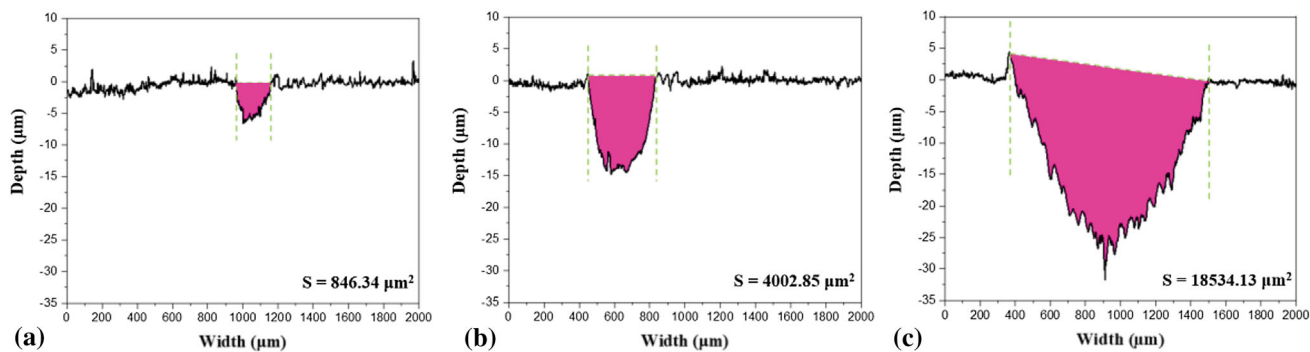

Fig. 10 Wear depth profiles during the 500 m sliding at 0.1 m/s velocity and under (a) 2 N, (b) 7 N, and (c) 12 N loads

Table 5 Volume loss and wear rates of the coated sample under different loads

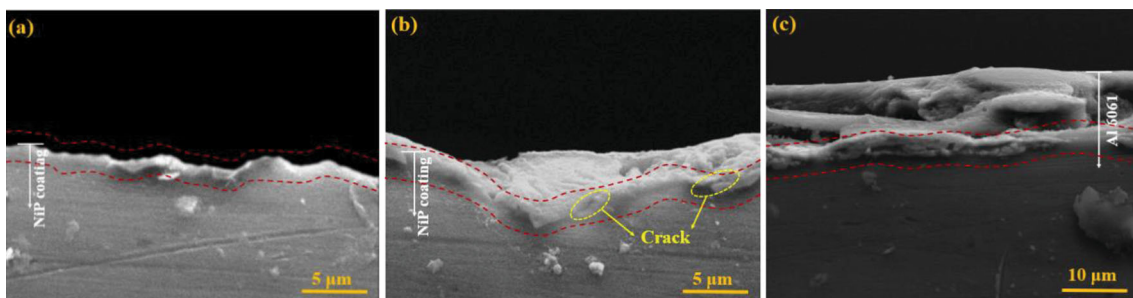| Load, N	r, mm	S, μm^2	V, mm³	L, m	W, mm³/N m
(a) 2	10	846.34 ± 15.6	$5.31 \times 10^{-2} \pm 1.25 \times 10^{-3}$	500	$5.45 \times 10^{-5} \pm 1.2 \times 10^{-6}$
(b) 7	10	4002.85 ± 83.2	$25.1 \times 10^{-2} \pm 8.3 \times 10^{-3}$	500	$7.18 \times 10^{-5} \pm 4.1 \times 10^{-6}$
(c) 12	10	18534.13 ± 342.82	$116.39 \times 10^{-2} \pm 41 \times 10^{-3}$	500	$19.4 \times 10^{-5} \pm 7.7 \times 10^{-6}$

Fig. 11 Cross-sectional SEM images of the wear tracks during the 500 m sliding at 0.1 m/s velocity and under (a) 2 N, (b) 7 N, and (c) 12 N loads

Table 6 Analysis of variance for wear depth and COF

Response	Source	DF	Adj SS	Adj MS	F-Value	P-Value
Wear depth	Regression	9	1095.27	121.697	2295.2	0.000
	Residual error	10	0.53	0.053		
	Lack-of-fit	5	0.4	0.08	3.13	
	Pure error	5	0.13	0.026		
	Total	19	1095.8			
COF	Regression	9	0.229738	0.025526	18.71	0.000
	Residual error	10	0.013642	0.001364		
	Lack-of-fit	5	0.005108	0.001022	0.6	
	Pure error	5	0.008533	0.001707		
	Total	19	0.24338			

DF: degrees of freedom, Adj SS: adjusted sum of squares, Adj MS: adjusted mean of squares

Table 7 Values of the determination coefficient (R^2) and adjusted determination coefficient (R^2_{adj})

Response	R^2	$R^2_{(adj)}$
Wear depth	99.95%	99.91%
COF	94.39%	89.35%

and local delamination resulted in the spalling and rupture of the films. Furthermore, the third-body abrasive wear occurred due to the formation of debris (Ref 39). The activation of this kind of wear can be confirmed based on the observation of the fluctuations in the friction coefficients (Fig. 6), as reported by others (Ref 51).

It has been reported that the wear debris can cause an improvement in the wear resistance based on the surface conditions and reaction with the environment (Ref 52). Also, it has been reported that TiN can react with oxygen during wear tests, and the formation of TiO_2 can make smooth surfaces (Ref 53). It needs to mention that decreasing the oxygen level can be due to removing the oxide film by increasing the load, as illustrated in Fig. 7. The formation of the oxide layer has also been supported in the work by Arulvel et al. (Ref 41) on the wear mechanisms of NiP coatings. They have stated that the adhesion of the oxide layer for NiP coatings during 500 m sliding is due to the presence of enough pressure ($\sim$ 5 N to 7 N) on the ball.

The wear depth profiles of the coated sample under various loads after 75 m and 500 m sliding are shown in Fig. 9 and 10. As shown in Fig. 9, it was difficult to measure the depth in the wear track at 2 N and 7 N loads after the 75 m sliding, but for 12 N load, the depth of the wear track was about 12 μm. For 500 m sliding, the volume loss ($V = 2.r.\pi.S$) and wear rate ($W = \frac{V}{N.L}$) were calculated (Ref 54) and listed in Table 5. In these equations, r is the radius of the wear tracks, S is the cross-sectional area of the wear depth profiles obtained using OriginPro 2018, N is the normal applied load, and L is the sliding distance. The results showed that increasing the load led to increasing the wear depth, wear width and wear rate. The existence of non-uniformity and serrated shape of the wear scar under the 12 N load can be due to the higher roughness of the worn surfaces and the occurrence of plowing and abrasive wear.

The surface did not suffer from severe wear under the load of 2 N, according to high magnification SEM images of the cross-sections of the coatings (Fig. 11). Mild wear of the NiP coating and minor plastic deformation was seen at 7 N load. Under 12 N load, the complete removal of the coatings with extensive plastic deformation and plowed area were observed.

3.4 Analysis of Variance

According to the ANOVA results in Table 6, it can be seen that the predictabilities of all models were at the 95% confidence level, and the developed models can be used for future applications. The adequacies of models were assessed, as shown in Table 7, with the determination coefficient R^2 and the adjusted determination coefficient R^2_{adj}. The closeness of R^2 to 1 indicated that the models fit well. The values of R^2_{adj} were also high, illustrating the prediction capacity of the models (Ref 55).

3.5 Statistical Modelling for Wear Depth and COF

Non-linear regression equations developed for responses are given in Eq 4 and 5. The regression equations were presented in the coded units by deleting non-significant terms based on the P-values. As can be seen from the equations, the linear terms had more effect on responses when compared to square and interaction terms.

$$Weardepth = 14.5184 + 7.6614*A - 1.3889*B + 3.4618*C + 1.6975*A^2 + 0.2126*B^2 + 0.7429*C^2 - 1.2750*A*B + 2.35*A*C$$

(Eq 4)

$$COF = 0.4169 + 0.10664*A + 0.04333*C - 0.0319*C^2 + 0.0513*A*C$$

(Eq 5)

Figure 12(a) and (b) presents the normal plots of the various parameters. It can be seen that the farther the factors from the line, the more significant their influence on the response. Factors with negative coefficients were shown on the left-hand side of the normal probability line and presented the negative effects. In contrast, the factors on the right had a positive effect. By comparing the results based on Fig. 12, it can be deduced that the effect of the load was more predominant, whereas the
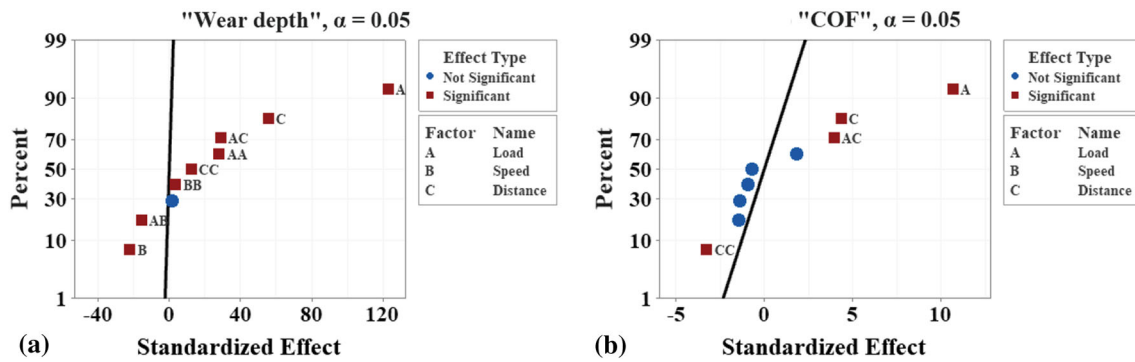
Fig. 12 Normal plots of the standardized effects of the factors on (a) Wear depth and (b) COF
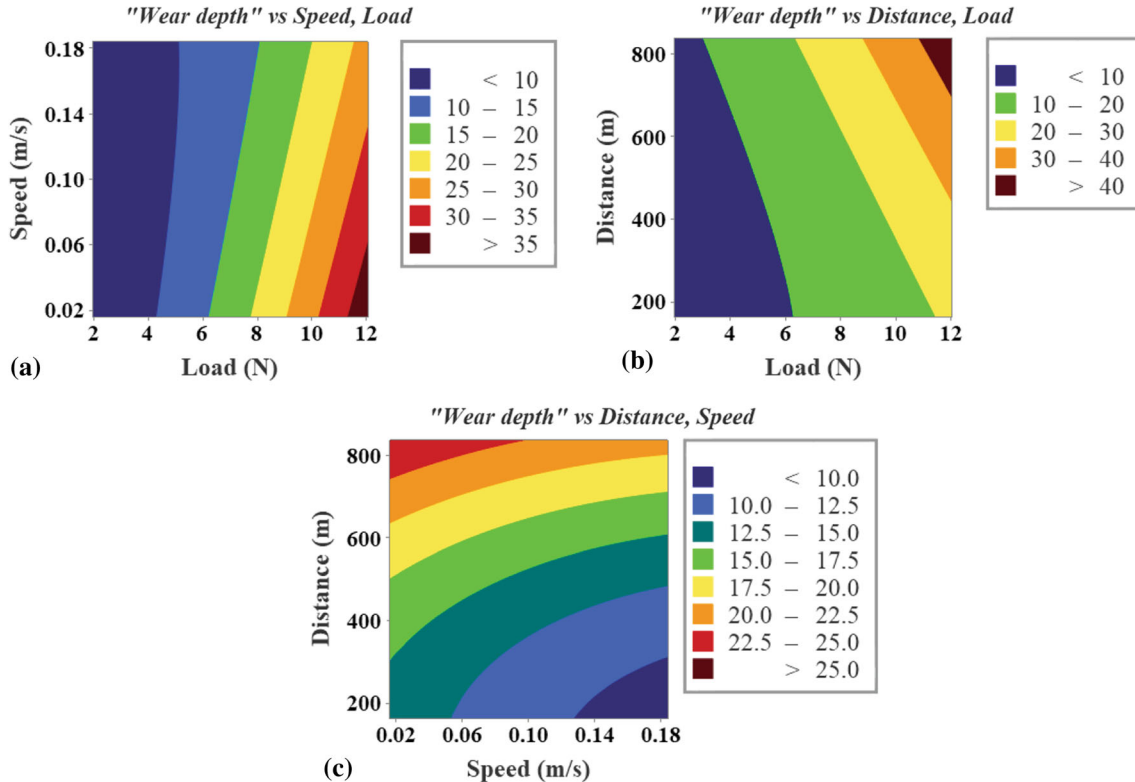

Fig. 13 Relative effects of (a) load and sliding speed, (b) load and sliding distance, and (c) sliding speed and sliding distance on the wear depth

sliding velocity had the most negligible impact on the wear depth and friction coefficient.

3.6 Interaction Effect of the Responses by Counter plots

The counterplots are presented to identify the responses and their interaction effects in Fig. 13 and 14. The plots were obtained by various combinations of load-speed, load-distance, and speed-distance, with the third independent parameter being kept at the center point. Different ranges of the responses were determined by changing the colors in plots. Figure 13(a) shows the graphical representation of the wear depth based on the applied load and sliding velocity. This graph confirmed that the wear depth was decreased as the load was reduced insofar as the dark blue region (wear depth < 10 μm) was observed at loads below 4 N for any speed; Therefore, the effect of velocity

was almost negligible in this plot. According to Fig. 13b, increasing the load and distance led to the rise of the wear depth. Figure 13c demonstrates that the maximum wear depth occurred with the decrease in the sliding velocity at the higher sliding distance.

According to Fig. 14a, representing the COF map based on load-speed, the effect of velocity was negligible, and COF was < 0.4 in the load ranges of 4 N to 6 N. Also, at very low loads, even over long distances, the COF was low (Fig. 14b). Figure 14c shows that at distances more than 450 meters and speeds below 0.15, the COF was above 0.4.

As the involved surfaces progressed towards each other with increasing the load, the contact area of asperities and the involved surfaces in contact were increased; as a result, the wear mass loss by the counterface material was raised, causing the rise of the wear depth. The wear debris removal mecha-
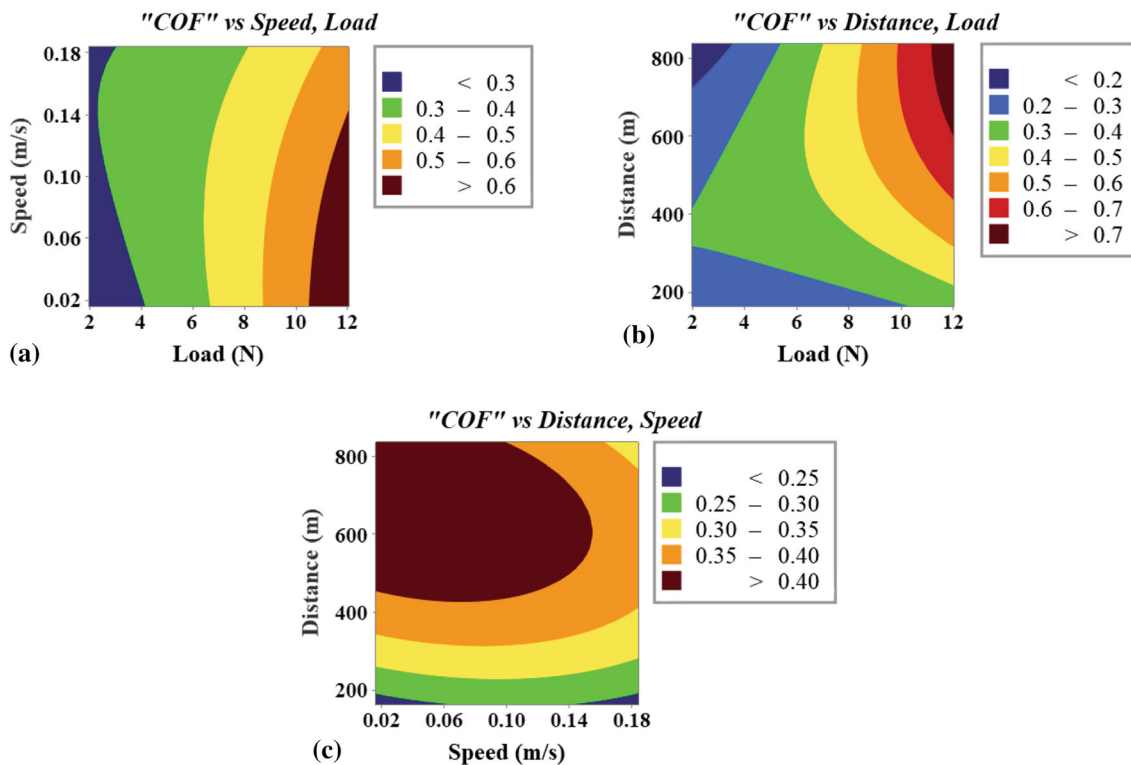
Fig. 14 Relative effects of (a) load and sliding speed, (b) load and sliding distance, and (c) sliding speed and sliding distance on COF

nisms caused by different slip conditions (different load, speed, and distance), can determine the level of the worn surfaces of the coatings after the ball-on-disk test (Ref 56). At low levels of loads and distances, the rolling effect induced by the worn particles of the debris was stuck between the counterface and coating, causing the lower wear; however, by increasing these two parameters, this effect disappeared, leading to plowing and a greater wear depth (Ref 57). The wear depth was increased by increasing the loads more than 10 N. On the other hand, the higher levels of the sliding distance led to the rise of the temperature; this, in turn, led to more severe deformations, thus enlarging the region and wear depth (Ref 55).

Regarding the values of wear depth, the NiP intermediate layer was mainly observed after the tests. The softening phenomenon might have occurred at high speeds due to the increased temperature; the nickel-phosphorus film was softened, thus acting as a lubricant layer; then the friction between contact surfaces and the amount of wear were reduced. In fact, this layer acted as a tribolayer. As discussed earlier, the presence of oxygen on the damaged surfaces in the EDS Spectra (Fig. 7 and 8) evidenced this phenomenon. The pressure exerted by the ball and the presence of strong intermolecular forces contributed to the adhesion of the tribolayer. Enough adhesion of the tribolayer promoted the wear resistance. At high loads, the pressure of the ball on the tribolayer was increased, eventually plowing and destroying it (Ref 41). Therefore, at a higher sliding speed, until the tribolayer remains intact, the surface contact between the zirconia ball and specimen is decreased, thus reducing the wear.

4. Conclusions

This work investigated the influence of various parameters on the dry sliding wear behavior of the Al 6061 alloy substrate coated by the NiP/TiN coating against the zirconia ball using the Response Surface Method (RSM). The following conclusions could be drawn:

1. The NiP and TiN layers were successfully fabricated on the surface of an aluminum substrate. Results confirmed that the Ni_3P crystalline phase was formed after heat treatment of the NiP coating.
2. Applying the duplex coating of NiP/TiN on the aluminum substrate improved the hardness by 24 times; however, the surface roughness was also increased.
3. At a constant distance and velocity, the mean friction coefficient was enhanced by increasing the load. Under 2 N load, the damage was relatively slight, whereas, at the 7 N load, heavier wear was observed. With increasing the load to 12 N, both coatings were completely damaged and the abrasive wear was the main mechanism accounting for the wear process.
4. Based on the design of experiments data, R^2 had a value of 99.95% for wear depth and a value of 94.39% for COF. The developed model can be used for predicting future values with minimum errors.
5. The applied load was the most important factor in the wear depth and COF. Moreover, the decrease of velocity helped to increase these two responses.

References

1. A.E. Somers, P.C. Howlett, J. Sun, D.R. MacFarlane, M. Forsyth, Transition in Wear Performance for Ionic Liquid Lubricants Under Increasing Load, *Tribol. lett.*, 2010, **40**(2), p 279–284.

2. M. Javidikia, M. Sadeghifar, V. Songmene, M. Jahazi, On the Impacts of Tool Geometry and Cutting Conditions in Straight Turning of Aluminum Alloys 6061–T6: An Experimentally Validated Numerical Study, *Int. J. Adv. Manuf. Technol.*, 2020, **106**(9), p 4547–4565.

3. Z. Chen, G. Fang, J.-Q. Zhao, Formability Evaluation of Aluminum Alloy 6061–T6 Sheet at Room and Elevated Temperatures, *J. Mater. Eng. Perform.*, 2017, **26**(9), p 4626–4637.

4. R.-j. Fan, S. Attarilar, M. Shamsborhan, M. Ebrahimi, G. Ceren, H.V. ÖZKAVAK, Enhancing Mechanical Properties and Corrosion Performance of AA6063 Aluminum Alloys Through Constrained Groove Pressing Technique, Trans. Nonferrous Met. Soc. China., 2020, 30(7), p 1790-1802

5. H. Wang, T. Zhang, S. Wang, S. To, Characterization of the Friction Coefficient of Aluminum Alloy 6061 in Ultra-Precision Machining, Met., 2020, 10(3), p 336

6. X. Meng, Y. Huang, S. Liu, Y. Xie, J. Li, L. Zhou, Functionally Gradient Coating of Aluminum Alloy via in situ arc Surface Nitriding with Subsequent Friction Stir Processing, Adv. Eng. Mater., 2019, 21(1), p 1800841

7. D. Kumar, K. Pandey, Experimental Investigations of Sol-Gel Process Parameters for Wear Reduction on Thermal Barrier Coated AA2024 Aluminum Alloys with the Use of Taguchi-Based Optimization, *Sadhana*, 2020, **45**(1), p 1–12.

8. M. Kocabaş, C. Örnek, M. Curioni, N. Cansever, Nickel Fluoride as a Surface Activation Agent for Electroless Nickel Coating of Anodized AA1050 Aluminum Alloy, *Surf. Coat. Technol.*, 2019, **364**, p 231–238.

9. I. Ali, M. Quazi, E. Zalnezhad, A.A. Sarhan, N.L. Sukiman, M. Ishak, Hard Anodizing of Aerospace AA7075-T6 Aluminum Alloy for Improving Surface Properties, *Trans. Indian Inst. Met.*, 2019, **72**(10), p 2773–2781.

10. T. Polcar, A. Cavaleiro, High Temperature Behavior of Nanolayered CrAlTiN Coating: Thermal Stability, Oxidation, and Tribological Properties, *Surf. Coat. Technol.*, 2014, **257**, p 70–77.

11. M. Hua, H. Ma, C. Mok, J. Li, Tribological Behavior of Patterned PVD TiN Coatings on M2 Steel, *Tribol. Lett.*, 2004, **17**(3), p 645–653.

12. F. Zhou, Y. Wang, F. Liu, Y. Meng, Z. Dai, Friction and Wear Properties of Duplex MAO/CrN Coatings Sliding Against Si3N4 Ceramic Balls in Air, Water and Oil, *Wear*, 2009, **267**(9–10), p 1581–1588.

13. J.A.-B. Wilson, S. Banfield, J. Eichler, A. Leyland, A. Matthews, J. Housden, An investigation into the Tribological Performance of Physical Vapour Deposition (PVD) Coatings on High Thermal Conductivity Cu-Alloy Substrates and the Effect of an Intermediate Electroless Ni–P Layer Prior to PVD Treatment, *Thin Solid Films*, 2012, **520**(7), p 2922–2931.

14. C. Donnet, A. Erdemir, Solid Lubricant Coatings: Recent Developments and Future Trends, *Tribol. Lett.*, 2004, **17**(3), p 389–397.

15. M. Staia, E.P. Cabrera, A. Iost, A. Zairi, S. Belayer, A. Van Gorp, Tribological Response of AA 2024–T3 Aluminium Alloy Coated with a DLC Duplex Coating, *Tribol. Int.*, 2015, **85**, p 74–87.

16. Y.-Y. Li, Y.-C. Hsiao, C.-C. Wu, F.-B. Wu, Phase Transformation, Thermal Stability and Indentation Behavior of Sputtering Ni-P-Based Interlayer Enhanced CrN Composite Coatings, *Surf. Coat. Technol*, 2009, **204**(6–7), p 1002–1007.

17. C.-K. Lin, C.-H. Hsu, S.-C. Kung, Effect of Electroless Nickel Interlayer on Wear Behavior of CrN/ZrN Multilayer Films on Cu-Alloyed Ductile Iron, *Appl. Surf. Sci.*, 2013, **284**, p 59–65.

18. F.-B. Wu, J.-J. Li, J.-G. Duh, Evaluation of the Mechanical Properties and Tribological Behavior of the CrN Coating Deposited on Mild Steel Modified with Electroless Ni Interlayer, *Thin Solid Films*, 2000, **377**, p 354–359.

19. C.-H. Hsu, K.-L. Chen, J.-H. Lu, Effects of Electroless Nickel Interlayer on Surface Properties of CrN Arc-Coated Austempered Ductile Iron, *Surf. Coat. Technol*, 2008, **203**(5–7), p 868–871.

20. S. Suresh, N.S.V. Moorthi, S. Vettivel, N. Selvakumar, Mechanical Behavior and Wear Prediction of Stir Cast Al–TiB2 Composites Using Response Surface Methodology, *Mater. Des.*, 2014, **59**, p 383–396.

21. N. Mandal, H. Roy, B. Mondal, N. Murmu, S. Mukhopadhyay, Mathematical Modeling of Wear Characteristics of 6061 Al-alloy-SiCp Composite Using Response Surface Methodology, *J. Mater. Eng. Perform.*, 2012, **21**(1), p 17–24.

22. N. Radhika, R. Raghu, Dry Sliding Wear Behaviour of Aluminium Al–Si12Cu/TiB 2 Metal Matrix Composite Using Response Surface Methodology, *Tribol. Lett.*, 2015, **59**(1), p 1–9.

23. L. Zhou, L. Luo, R. Wang, J. Zhang, Y. Huang, X. Song, Process Parameter Optimization in Refill Friction Spot Welding of 6061 Aluminum Alloys Using Response Surface Methodology, *J. Mater. Eng. Perform.*, 2018, **27**(8), p 4050–4058.

24. S. Vettivel, N. Selvakumar, R. Narayanasamy, N. Leema, Numerical Modelling, Prediction of Cu–W Nano Powder Composite in Dry Sliding Wear Condition Using Response Surface Methodology, *Mater. Des.*, 2013, **50**, p 977–996.

25. D. Jhodkar, M. Amarnath, H. Chelladurai, J. Ramkumar, Experimental Investigations to Study the Effects of Microwave Treatment Strategy on Tool Performance in Turning Operation, *J. Mater. Eng. Perform.*, 2018, **27**(12), p 6374–6388.

26. I. Saravanan, A.E. Perumal, S. Vettivel, N. Selvakumar, A. Baradeswaran, Optimizing wear behavior of TiN coated SS 316L against Ti alloy using Response Surface Methodology, *Mater. Des.*, 2015, **67**, p 469–482.

27. I. Saravanan, A.E. Perumal, R.F. Issac, Wear Study of Cross Linked UHMWPE Hybrid Composite-TiN Interface, *Surf. Interfac.*, 2016, **4**, p 42–50.

28. A. Leyland, M. Bin-Sudin, A. James, M. Kalantary, P. Wells, A. Matthews, J. Housden, B. Garside, TiN and CrN PVD COATINGS on Electroless Nickel-Coated Steel Substrates, *Surf. Coat. Technol.*, 1993, **60**(1–3), p 474–479.

29. C. Subramanian, G. Cavallaro, G. Winkelman, Wear Maps for Titanium Nitride Coatings Deposited on Copper and Brass with Electroless Nickel Interlayers, *Wear*, 2000, **241**(2), p 228–233.

30. D. Ahmadkhaniha, F. Eriksson, C. Zanella, Optimizing Heat Treatment for Electroplated NiP and NiP/SiC Coatings, COATINGS, 2020, 10(12), p 1179

31. I. Apachitei, F. Tichelaar, J. Duszczyk, L. Katgerman, The Effect of Heat Treatment on the Structure and Abrasive Wear Resistance of Autocatalytic NiP and NiP–SiC Coatings, *Surf. Coat. Technol.*, 2002, **149**(2–3), p 263–278.

32. V. Vitry, A.-F. Kanta, F. Delaunois, Mechanical and Wear Characterization of Electroless Nickel-Boron Coatings, *Surf. Coat. Technol.*, 2011, **206**(7), p 1879–1885.

33. G. Singh, S.L.-I. Chan, N. Sharma, Parametric Study on the Dry Sliding Wear Behaviour of AA6082–T6/TiB 2 in situ Composites Using Response Surface Methodology, J. Braz. Soc. Mech. Sci. Eng., 2018, 40(6), p 310

34. G.T.P. Azar, C. Yelkarasi, M. Ürgen, The Role of Droplets on the Cavitation Erosion Damage of TiN Coatings Produced with Cathodic Arc Physical Vapor Deposition, *Surf. Coati. Technol.*, 2017, **322**, p 211–217.

35. P. Panjan, M. Čekada, M. Panjan, D. Kek-Merl, Growth Defects in PVD Hard Coatings, *Vacuum*, 2009, **84**(1), p 209–214.

36. M. Buchtík, L. Doskočil, R. Brescher, P. Doležal, J. Másilko, J. Wasserbauer, The Effect of Crystallization and Phase Transformation on the Mechanical and Electrochemical Corrosion Properties of Ni-P Coatings, Coatings, 2021, 11(4), p 447

37. P. Sahoo, Optimization of Electroless Ni-P Coatings Based on Multiple Roughness Characteristics, *Surf. Interface Anal.*, 2008, **40**(12), p 1552–1561.

38. S. Sarkar, A. Mukherjee, R.K. Baranwal, J. De, C. Biswas, G. Majumdar, Prediction and Parametric Optimization of Surface Roughness of Electroless Ni-Co-P Coating Using Box-Behnken Design, *J Mech. Behav. Mater.*, 2019, **28**(1), p 153–161.

39. M. Falsafein, F. Ashrafizadeh, A. Kheirandish, Influence of Thickness on Adhesion of Nanostructured Multilayer CrN/CrAlN Coatings to Stainless Steel Substrate, *Surf. Interf.*, 2018, **13**, p 178–185.

40. M. Bashir, M. Shafiq, M. Naeem, M. Zaka-ul-Islam, J. Díaz-Guillén, C. Lopez-Badillo, M. Zakaullah, Enhanced Surface Properties of Aluminum by PVD-TiN Coating Combined with Cathodic Cage Plasma Nitriding, *Surf. Coat. Technol.*, 2017, **327**, p 59–65.

41. S. Arulvel, A. Elayaperumal, M. Jagatheeshwaran, Controlling Adhesive Wear Failure of Nickel-Phosphorus Coating at High Load Condition Using Crab Shell Particle as Reinforcement, *Eng. Fail. Anal.*, 2018, **90**, p 310–323.

42. M. Ebrahimian-Hosseinabadi, K. Azari-Dorcheh, S.M. Vaghefi, Wear Behavior of Electroless Ni–P–B₄C Composite Coatings, *Wear*, 2006, **260**(1–2), p 123–127.

43. M. Palaniappa, S. Seshadri, Friction and Wear Behavior of Electroless Ni–P and Ni–W–P Alloy Coatings, *Wear*, 2008, **265**(5–6), p 735–740.

44. O. León, M. Staia, H. Hintermann, High Temperature Wear of an Electroless Ni–P–BN (h) Composite Coating, *Surf. Coat. Technol.*, 2003, **163**, p 578–584.

45. R. Guo, C. Zhang, Y. Yang, Y. Peng, L. Liu, Corrosion and Wear Resistance of a Fe-based Amorphous Coating in Underground Environment, *Intermetallics*, 2012, **30**, p 94–99.

46. N. Ghavidel, S.R. Allahkaram, R. Naderi, M. Barzegar, H. Bakhshandeh, Corrosion and Wear Behavior of an Electroless Ni-P/nano-SiC Coating on AZ31 Mg Alloy Obtained Through Environmentally-Friendly Conversion Coating, Surf. Coat. Technol., 2020, 382, p 125156

47. W. Fu, Q.-Y. Chen, C. Yang, D.-L. Yi, H.-L. Yao, H.-T. Wang, G.-C. Ji, F. Wang, Microstructure and Properties of High Velocity Oxygen Fuel Sprayed (WC-Co)-Ni Coatings, *Ceram. Int.*, 2020, **46**(10), p 14940–14948.

48. R. Soleimani, F. Mahboubi, M. Kazemi, S. Arman, Corrosion and Tribological Behaviour of Electroless Ni–P/nano-SiC Composite Coating on Aluminium 6061, *Surf. Eng.*, 2015, **31**(9), p 714–721.

49. X. Shu, Z. He, Y. Wang, L. Yin, Mechanical Properties of Ni-Based Coatings Fabricated by Electroless Plating Method, *Surf. Eng.*, 2020, **36**(9), p 944–951.

50. S. Ghasemi, A. Shanaghi, P.K. Chu, Nano Mechanical and Wear Properties of Multi-layer Ti/TiN Coatings Deposited on Al 7075 by High-Vacuum Magnetron Sputtering, *Thin Solid Films*, 2017, **638**, p 96–104.

51. E. Arslan, Y. Totik, E.E. Demirci, I. Efeoglu, Wear and Adhesion Resistance of Duplex Coatings Deposited on Ti6Al4V Alloy Using MAO and CFUBMS, *Surf. Coat. Technol.*, 2013, **214**, p 1–7.

52. M. Allahyarzadeh, M. Aliofkhazraei, A.S. Rouhaghdam, H. Alimadadi, V. Torabinejad, Mechanical Properties and Load Bearing Capability of Nanocrystalline Nickel-Tungsten Multilayered Coatings, Surf. Coat. Technol., 2020, 386, p 125472

53. S. Wilson, A. Alpas, Tribo-layer Formation During Sliding Wear of TiN Coatings, *Wear*, 2000, **245**(1–2), p 223–229.

54. Y. Zhang, F. Chen, Y. Zhang, C. Du, Influence of Graphene Oxide Additive on the Tribological and Electrochemical Corrosion Properties of a PEO Coating Prepared on AZ31 Magnesium Alloy, Tribol. Int., 2020, 146, p 106135

55. I. Saravanan, A.E. Perumal, R.F. Issac, S. Vettivel, A. Devaraju, Optimization of Wear Parameters and Their Relative Effects on TiN Coated Surface Against Ti6Al4V Alloy, *Mater. Des.*, 2016, **92**, p 23–35.

56. J.S. Grewal, B.S. Sidhu, S. Prakash, Effect of Sliding Velocity on Wear Behaviour of TiAlN Coatings, Advanced Materials Research, 2016, Trans. Tech. Publ., pp 24-38

57. A. Mukhopadhyay, S. Duari, T.K. Barman, P. Sahoo, Investigation of Wear Behavior of Electroless Ni-PW Coating Under Dry and Lubricated Conditions Using RSM and Fuzzy Logic, *Port. Electrochim. Acta*, 2016, **34**(4), p 231–255.